Case Studies in Construction Materials 20 (2024) e03144

Contents lists available at ScienceDirect

Case Studies in Construction Materials

journal homepage: www.elsevier.com/locate/cscm

Case study

Assessment of steel-fiber-reinforced segmental lining of Chamshir water conveyance tunnel, Iran: Integrating laboratory experiments, field observations, and numerical analysis

Mohammad Ezazi [a,1], Mohammad Farouq Hossaini [b], Rasoul Sheikhmali [c,2], Mohammad Khosrotash [d,3], Ebrahim Sharifi Teshnizi [e,4], Brendan C. O'Kelly [f,*,5]

[a] School of Mining Engineering, College of Engineering, University of Tehran, 1439957131, Iran
[b] School of Mining Engineering, College of Engineering, University of Tehran, 1417935840, Iran
[c] Department of Civil Engineering, University of Calgary, T2N 1N4, Canada
[d] Tunnel Rod Consulting Eng. Inc, 1481635453, Iran
[e] Department of Geology, Faculty of Science, Ferdowsi University of Mashhad, P.O. Box 91775-1436, Mashhad, Iran
[f] Department of Civil, Structural and Environmental Engineering, University of Dublin, Trinity College, Dublin D02 PN40, Ireland

ARTICLE INFO

Keywords:
Segmented lining
Reinforced concrete
Steel fibers
Finite element analysis
Concrete damage

ABSTRACT

The conventional rebar-reinforced concrete (RRC) segmented lining of the Chamshir water conveyance tunnel (CWCT) in Bushehr Province, Iran, has experienced significant damage issues. This paper presents a comprehensive study involving laboratory experiments, numerical simulations and statistical site-survey analysis aimed at evaluating the mechanical behaviors and structural integrity of steel fiber-reinforced concrete (FRC) and fiber-rebar-reinforced concrete (FRRC) segment types, as compared to the traditional RRC segments. Laboratory compressive, tensile and flexural strength testing provided insights into the impacts of the fiber diameter and content on the ultimate strength capacities of the FRC test specimens. Numerical simulations scrutinized beam and segment models reinforced by the explicit inclusion of traditional rebar and/or randomly orientated and evenly distributed steel fiber reinforcements. The segment simulations were directed at investigating concentrated loading, representative of the jack thrust force applied in installing the segments during the tunnel boring machine (TBM) installation phase. Additionally, a field-monitoring program of the CWCT lining quantified common damage patterns among 545 RRC and 416 FRC segments that had experienced damage during their installation and in-service phases. For FRC beams, increased fiber content correlated with enhanced strength capacity, although the use of larger diameter fibers produced diminishing returns. Compared to the considerable damage expected near the applied TBM jack thrust force for the RRC segments, significantly reduced damage was predicted for both the FRC and FRRC segment types. However, even modest jack force misalignment (of 5–7.5°) led to cracking damage

* Corresponding author.
E-mail addresses: mohammad.ezazi@ut.ac.ir (M. Ezazi), mfarogh@ut.ac.ir (M.F. Hossaini), rasoul.sheikhmali@ucalgary.ca (R. Sheikhmali), mo_khosrotash@yahoo.com (M. Khosrotash), Ebrahim.SharifiTeshnizi@mail.um.ac.ir (E. Sharifi Teshnizi), bokelly@tcd.ie (B.C. O'Kelly).
[1] ORCID: 0000-0003-1291-3601
[2] ORCID: 0000-0002-6247-8101
[3] ORCID: 0009-0003-2094-8907
[4] ORCID: 0000-0001-9574-4149
[5] ORCID: 0000-0002-1343-4428

https://doi.org/10.1016/j.cscm.2024.e03144
Received 2 February 2024; Received in revised form 24 March 2024; Accepted 7 April 2024
Available online 8 April 2024

across the segment width for all models, although with the fibers included, the chipping damage was reduced substantially. The findings underscore the potential of FRC and FRRC segment types to achieve better structural integrity compared to traditional RRC segments.

1. Introduction

Tunnel boring machine (TBM) technology stands as a cornerstone of modern tunnel construction, distinguished for its efficiency and safety [1,2]. Within this domain, precast reinforced-concrete segmented linings serve as vital support structures. However, the lifecycle of these segments, from their fabrication to installation and service, is fraught with challenges, including susceptibility to damage [3,4]. While compressive stresses typically predominate, the concentrated loads acting during the segments' handling and installation phases can instigate tensile stresses, increasing the risks of splitting and spalling [5–15]. In addressing these vulnerabilities, researchers have sought alternatives to conventional steel reinforcement-bar (rebar), with a notable focus on incorporating steel fibers to augment mechanical behavior and structural integrity [16–26]. Recent decades have witnessed a surge in the use of fibers in concrete mixes for structural purposes [13,24,27–34]. These fibers hold the promise of enhancing post-cracking tensile behavior and toughness capacity [15,35–43]. Various experimental programs have explored the influence of fiber parameters, e.g., diameter, aspect ratio, spatial distribution, and orientation, on the structural response [29,44–46]. Noteworthy among these studies is the evaluation by [46] of ultra-high-performance steel-fiber-reinforced concrete (FRC), demonstrating the potentials to enhance both mechanical and durability performances. Examples abound of tunnel linings constructed using FRC segments, including the Barcelona Metro Line 9, the Monte Lirio tunnel in Panama, and the Prague Metro line [2,13,16,24,47]. These instances underscore the effectiveness of FRC in tunnel construction and its increasing adoption. FRC segments present a particularly promising avenue for mitigating undesirable effects arising from the action of the TBM thrust jack(s) during their installation, and from seismic events in-service, with previous studies examining their mechanical and structural behaviors under varied loading conditions [21,27,38,48–54]. However, notwithstanding the availability of guidelines on FRC segmented lining design, the applicability of using FRC segments in place of conventional rebar-reinforced concrete (RRC) segments for specific tunneling works necessitates careful assessment, including accounting for geological variations and site-specific conditions [50].

The present case study investigates the implemented RRC and FRC segment types used in the construction of the Chamshir water conveyance tunnel (CWCT) lining. Our investigation aims to elucidate the impact of fiber inclusion on the mechanical properties and structural resilience, while also assessing the feasibility and advantages of partially substituting or complementing the rebar with fiber reinforcement (i.e., for fiber-rebar-reinforced concrete (FRRC)). While previous researchers often relied on equivalent constitutive laws in their numerical models, the innovative approach implemented in this study for simulating the physical inclusion of steel fibers

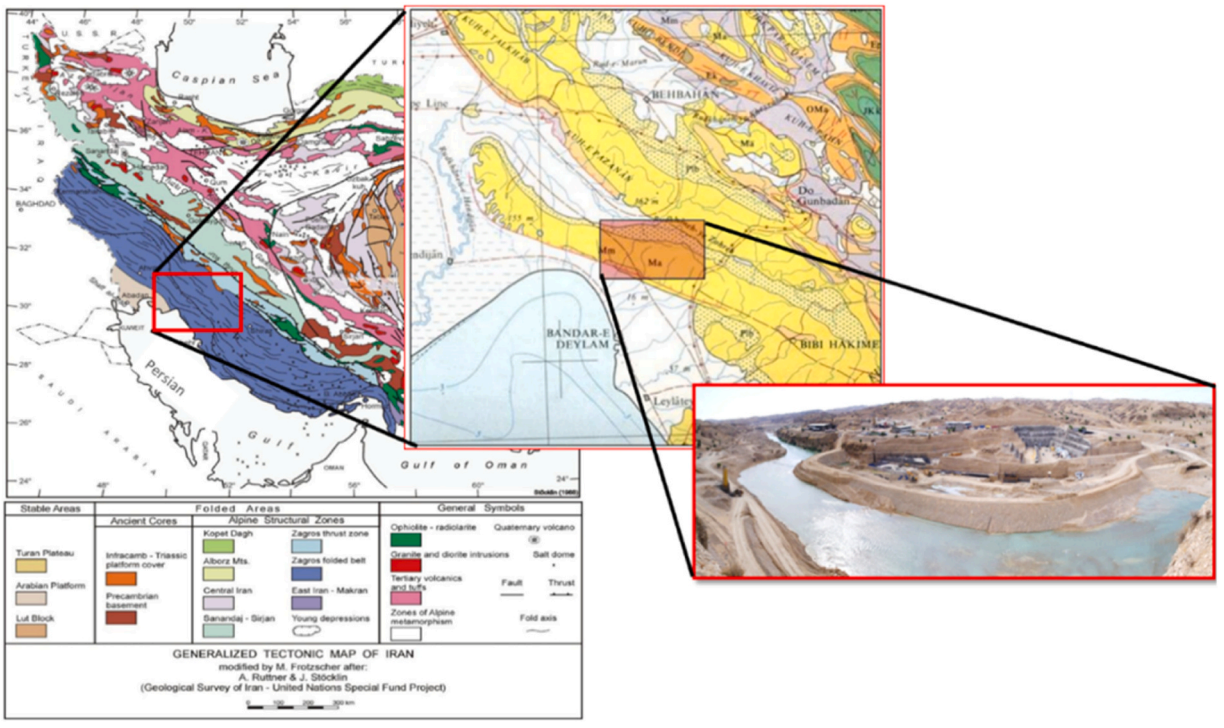

Fig. 1. General location and geology of the CWCT crossing beneath the Zohreh river [77,78].

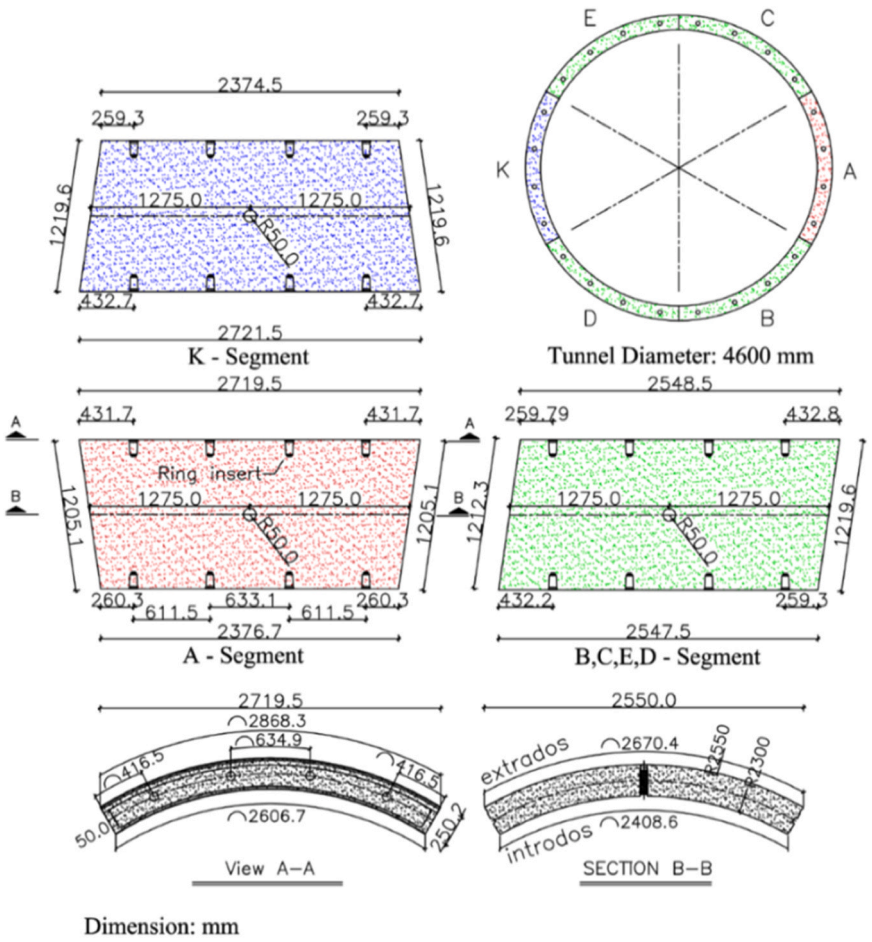

Fig. 2. Geometry of the six segments comprising the CWCT's ring lining.

in concrete for reinforcement purposes gives a more nuanced understanding of the fiber–concrete interactions. By capturing micro-mechanical properties and processes, such as damage initiation and evolution, the developed finite-element analysis (FEA) provides valuable insights for various applications, including the tunnel segmented lining. In the CWCT case study, we address this knowledge gap by meticulously modelling the steel fibers as being randomly oriented and evenly dispersed throughout the segments. Our investigation examines the mechanical attributes and structural integrity of variously loaded FRC components for three different fiber diameter sizes and fiber quantities (as proportions of the concrete mix investigated), and scrutinizes the damage initiation and progression in RRC, FRC, and FRRC segment types, with a focus on the role of the embedded fibers in damage mitigation. To achieve these goals, this paper presents the results of laboratory experiments, numerical simulations, as well as field observations and statistical analysis of observed damage patterns to in-situ RRC and FRC segment types of the CWCT lining, thereby obtaining a holistic understanding of the tunnel lining performance for the different reinforcement strategies. In synthesizing the laboratory experiment, numerical simulation and field observation results, this research bridges the gap between small-scale controlled laboratory testing conditions and the dynamic realities of tunnel construction. By amalgamating the various methodologies, the study aims to provide a robust basis for assessing the efficacy of fiber reinforcement and combined rebar and fiber reinforcements in enhancing the structural integrity of the segmented lining of the CWCT amidst diverse operational scenarios.

2. Case study — segmented lining of the Chamshir water conveyance tunnel (CWCT)

The CWCT is located downstream of the Chamshir dam, in the east of Bushehr province, southwest Iran. The tunnel itself is more than 7-km long, with an internal diameter of approximately 4.6 m. The area in which the tunnel is located occurs in the simply folded Zagros (SFZ) zone, with the geology shown in Fig. 1.

From Fig. 1, the main stratigraphic units, which outcrop in the project area, include the mudstones, marlstones, sandstones and siltstones of the Aghajari formation. This region includes very wide and gently folded parallel anticlines and synclines. In some synclines and the lower parts of anticline limbs, the Aghajari formation is covered by conglomerates and sandstones of the Bakhtiari formation and Quaternary deposits. The Bibi-Hakimeh anticline, with a NW-SE trend (parallel to the general trend of the SFZ zone), is

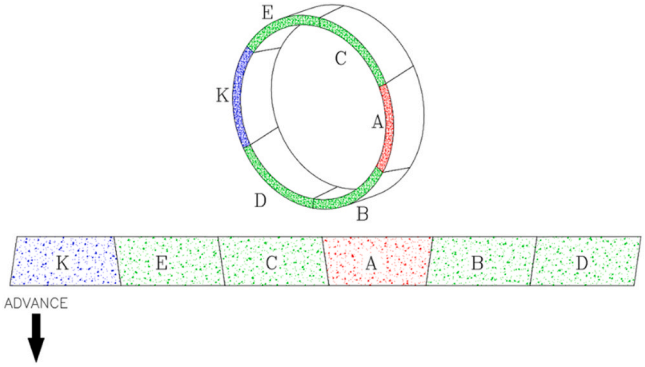

Fig. 3. Configuration and dimensions of the six trapezoidal segments (A–E and K) forming the CWCT's ring lining.

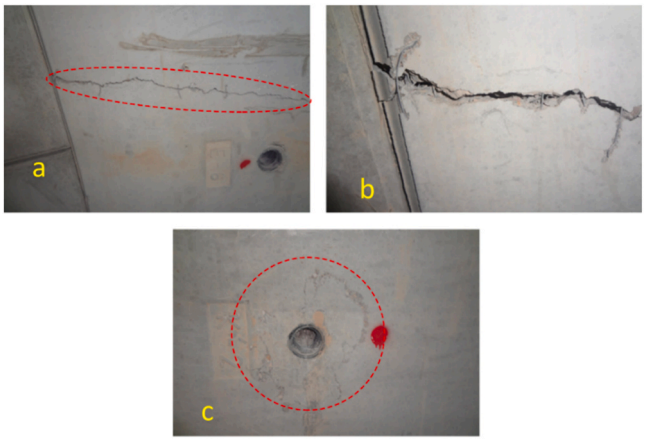

Fig. 4. Examples of damaged CWCT segments: (a) cross-width damage; (b) corner chipping; (c) center crumbling.

Fig. 5. Schematic plan of FRC mixture preparation.

the main structure in the project area (see Fig. 1) — the total 7-km length of the CWCT being covered in its northeastern limb. Geological site investigations did not identify any important fault zone along the CWCT's alignment.

Unlike the originally designed hexagonal shape, a trapezoidal-segmented tunnel lining was later adopted to provide better control over inward and outward water flows. Each lining ring is comprised of six separate 1.2-m long by 0.25-m-thick quadrilateral RRC or

Table 1
Physical characteristics of hooked-end steel fibers.

Feature	Type I	Type II	Type III
Length, L (mm)	50	50	50
Developed length*, L_D (mm)	55	55	55
Diameter, D (mm)	0.8	1.0	1.2
Aspect ratio, L/D	62.5	50.0	41.7
Number of fibers per kilogram	4830	3220	2200

* Actual fiber length after straightening.

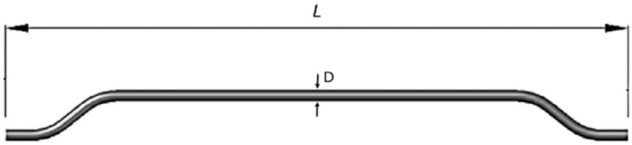

Fig. 6. Schematic geometry of single steel fiber.

Table 2
Composition of C40-Class concrete mix (per cubic meter of concrete).

Cement – Type II (kg)	Plasticizer – Optima-280 (% of volume)	Water (kg)	Sand (kg)	Fine gravel (kg)	Coarse gravel (kg)
470	0.56	162	1100	300	500

FRC segments (see Fig. 2), with the configuration of the six installed segments forming the lining ring illustrated in Fig. 3.

The conventional RRC segments that comprised the CWCT lining exhibited signs of significant damage having occurred during their installation, as evident from the images shown in Fig. 4. Such deterioration of the lining poses a substantial risk to the operational effectiveness of the tunnel's water conveyance system. To address and mitigate this detrimental occurrence, an alternative reinforcement approach of including both fiber reinforcement and traditional rebar [2,10,12,16,24,49] was devised and executed. This strategy was implemented for the CWCT with the objective of augmenting the structural resilience and operational efficacy of the segmented lining, particularly for the demanding conditions encountered during its installation.

3. Methodology

3.1. Laboratory testing

The laboratory experiments started with casting a diverse set of FRC test specimens (Fig. 5), incorporating 50-mm long hooked-ended steel fibers of different diameter sizes (i.e., 0.8, 1.0, and 1.2 mm) and for different fiber contents (FCs) of 30, 40, and 50 kg of the steel fibers per cubic meter of the final concrete mix plan. Some unreinforced concrete (UC) specimens were also prepared (as controls). Apart from their different fiber diameters and contents, the test specimens shared identical concrete mix composition. Note, the same concrete mix composition investigated here had been used in fabricating the RRC and FRC segments of the CWCT lining.

Table 1 and Fig. 6 provide detailed information on the geometry (length, diameter and aspect ratio) of the individual steel fibers, and also the numbers of fibers per kilogram mass considering the three different fiber diameters investigated. While Table 2 lists the composition of the C40-Class concrete mix investigated. Note that the FC additions of 30, 40, and 50 kg/m^3 of the final concrete mix plan equate to fiber volume fractions of 0.42%, 0.56%, and 0.69%, respectively.

After fully blending the dry concrete mixture, the water and admixture were introduced, and the entire wet mixture was thoroughly blended before being placed into the specimen molds. The desired compaction was achieved by vibration, applied for 30 s, as per the study by [55]. The test specimens were allowed to cure in water for 28 days at ambient laboratory temperature. At 28 days, the cured specimens were subjected to a program of strength testing, in accordance with the European standard EN 12390 [56–58], aimed at quantifying how the fiber diameter and content affected the FRC specimens' mechanical properties for various loading conditions. Each scenario was tested in triplicate, with the overall testing program comprised of 18 numbers of uniaxial compression tests on 15×15×15-cm cubic specimens, indirect tension (Brazilian) tests on 15-cm diameter by 30-cm-long cylindrical specimens, and three-point bend (flexural strength) tests on 10-cm-square × 50-cm-long prismatic specimens (i.e., a total of 54 individual strength tests).

3.2. Numerical simulations

The numerical simulations were aimed to provide insights into the performances of various rebar and/or fiber reinforcement schemes, investigated for the controlled loading condition of the laboratory three-point bend test (using beam models), as well as

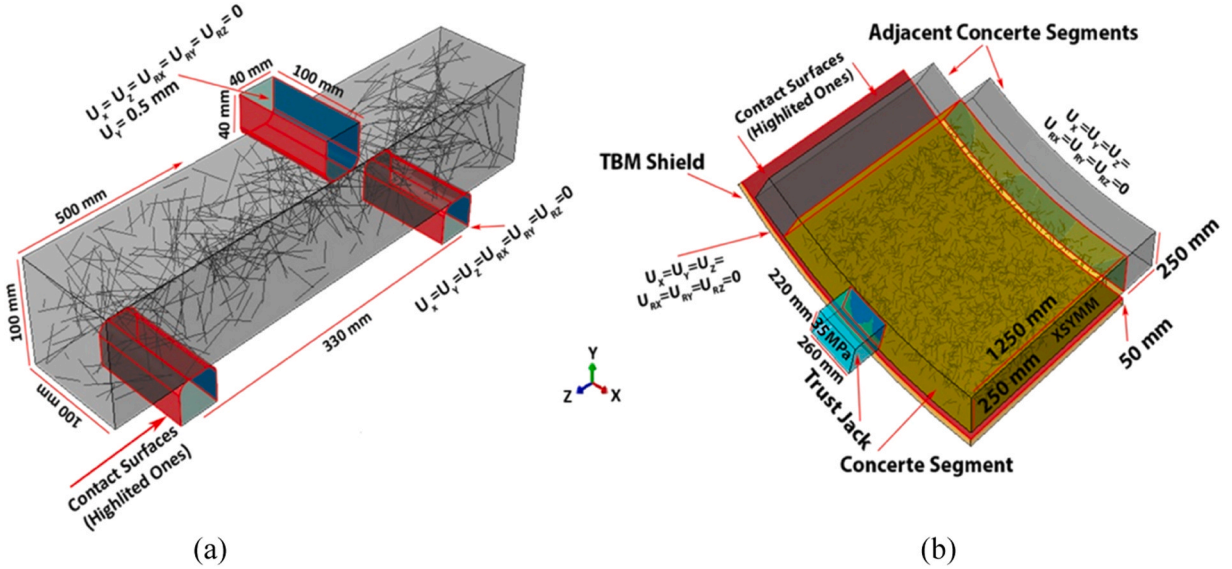

Fig. 7. Boundary conditions for the FRC-type beam and segment models: (a) three-point bend load test; (b) thrust force applied by single hydraulic jack over an area of 22×26-mm centered on the end surface of the 0.25-m-thick quadrilateral segment.

realistic in-situ loading scenarios of the TBM jack thrust force applied to the CWCT segments (investigated using segment models). To accomplish these, we used the powerful capabilities of the ABAQUS FEA software, which offers a wide range of material behaviors suitable for modeling diverse engineering applications. One of its notable features is the provision of explicit analysis capability, enabling modeling of large displacement/strain problems, with the Dynamic Explicit solver employed to solve the quasi-static problem investigated in the present research. Furthermore, ABAQUS provides users with a variety of contact features to model interaction problems between different parts of a model. These include the General Contact formulation, the Hard Contact property for modeling normal impenetrability of a mesh against another mesh, and Penalty/Coulomb tangential behavior employed for modeling friction between different parts of a model. Additionally, ABAQUS offers an embedding formulation for setting constraints between different parts or associated meshes. The software also provides access to a variety of finite-element types, with options for full or reduced integrations.

In our study, we meticulously designed the beam and segment models to incorporate both rebar and fiber reinforcements. While the rebar elements were directly sketched in ABAQUS, the embedded fibers were generated using MATLAB's uniformly distributed random function (unifrnd). This approach ensured our numerical models realistically reflected the actual distribution and orientations of the fibers within the physical C40-Class concrete beams/segments. In other words, for the models, each steel fiber was generated as a pair of points separated by a standardized distance of 50 mm (i.e., the fiber's physical length), with the fibers uniformly distributed and randomly orientated within the interior of the targeted beam or segment volume. The MATLAB code then exported these fibers in .inp file format, assigned them the beam element type of B31, and integrated them into the main .inp file generated by ABAQUS. Note, in this study, we used the eight-node linear brick, reduced integration, and hourglass-control element type of C3D8R for the host/concrete elements. Upon the fibers' importation into ABAQUS, further property assignments, assembly processes, and interaction definitions were performed. This meticulous approach ensured the realistic representation of the fiber reinforcement within the numerical models, enhancing the fidelity and reliability of our simulations.

To model the interactions and interfaces between the C40-Class concrete matrix and steel reinforcement (i.e., rebar and fiber) elements, we utilized the embedded element technique in ABAQUS. This technique allowed for the precise identification of geometric relationships between the nodes of the embedded elements and the host (i.e., concrete) elements. When a node of a reinforcement element was detected within a concrete element, its translational degrees of freedom (DOFs) were eliminated, thereby converting it into an embedded node. Subsequently, the translational DOFs of the embedded node were constrained to the interpolated values of the corresponding DOFs of the host element. Rotational DOFs were permitted for embedded elements (i.e., they were not constrained by the embedment process). This approach ensured the realistic representation of reinforcements within the concrete matrix, thereby enhancing the fidelity and reliability of our numerical models. Additionally, to model the interactions between the loading/reaction parts with the beams or segments, we implemented the General Contact formulation. This involved selecting surface pairs and assigning contact properties to ensure normal impenetrability (Hard Contact) and Penalty tangential behavior (friction coefficient of $\mu = 0.3$) conditions between different parts of a model.

Fig. 7 illustrates the dimensions, boundary conditions, and loading conditions considered for the beam and segment models.

For the beam models (see Fig. 7(a)), the bottom surfaces of the two supports (reaction pins) were fixed in all directions (i.e., no transitional or rotational DOFs). In the case of the central loading pin, all DOFs were prevented, except for its vertical transitional movement (along the *y*-axis direction) that was used to apply the displacement-controlled loading condition. When employing the

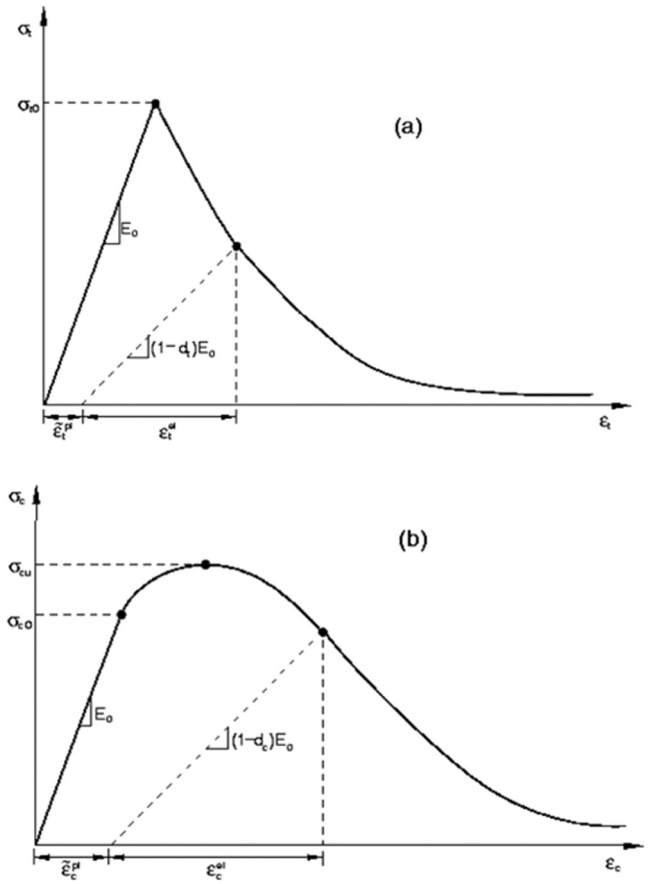

Fig. 8. Concrete damage plasticity model responses for uniaxial loading in (a) tension and (b) compression [61].

Table 3
Input parameters for concrete damage plasticity (CDP) model.

Elasticity		Auxiliary parameters of CDP model	
Bulk density (kg/m^3)	2500	σ_{b0}/σ_{c0}	1.12
Elastic modulus (GPa)	30	$\psi(\theta.f_i)$	38
Poisson's ratio	0.19	$\varepsilon(\theta.f_i)$	1
		K_c	0.666

Compression hardening		**Compression damage**	
σ_y (MPa)	ε_p	d_c	ε_p
14.99	0	0	0
20.19	0.0000491	0	0.0000502
29.99	0.0000649	0	0.000066
40.29	0.000101	0	0.000104
50	0.0005	0	0.000511
40.22	0.001679	0.2	0.001718
20.23	0.003726	0.6	0.003812
5.25	0.007704	0.9	0.007881

Tension stiffening		**Tension damage**	
σ_y (MPa)	ε_p	d_t	ε_p
1.75	0	0	0
2.5	0.0000193	0	0.0000193
1.644	0.00055	0.4	0.00550
0.758	0.000828	0.7	0.000828
0.199	0.001769	0.9	0.001769
0.0497	0.002703	0.95	0.002703

Table 4
Material properties of steel rebar and fibers obtained from direct-tension tests.

Reinforcement	Density (kg/m^3)	Elastic modulus (GPa)	Poisson's ratio	Yield stress (MPa)
Rebar	7200	200	0.2	345
Fibers	7200	192	0.2	1528

Table 5
Compressive, tension and flexural strengths mobilized for five FRC sample types investigated.

Property	UC	FRC1	FRC2	FRC3	FRC4	FRC5
Fiber diameter (mm)	–	0.8	0.8	0.8	1.0	1.2
Fiber content (kg/m^3)	–	30	40	50	40	40
Compressive strength (MPa)	52.19	52.39	61.70	59.50	60.90	56.26
	52.50	51.98	63.00	61.02	61.00	56.16
	51.98	52.50	64.20	61.10	60.14	56.37
Mean (MPa) =	52.22	52.29	62.97	60.54	60.68	56.26
Tensile (Brazilian) strength (MPa)	3.77	5.55	6.38	6.62	6.30	5.60
	4.48	5.40	6.56	6.54	5.85	5.71
	4.02	5.66	6.16	6.67	6.03	5.53
Mean (MPa) =	4.09	5.54	6.37	6.61	6.06	5.61
Flexural strength (MPa)	7.60	7.80	11.60	11.50	8.90	8.50
	8.00	9.50	12.00	12.00	8.50	8.00
	7.70	9.30	11.50	12.60	9.00	8.20
Mean (MPa) =	7.77	8.87	11.70	12.03	8.80	8.23

explicit analysis, for investigating a quasi-static problem we strive for a balance between the execution time/cost and the manipulation of the results. For instance, as the displacement amount (which can be also interpreted as the loading rate) is increased, the intended analysis will be completed in a shorter time, which is desirable. However, due to the inertia effect, the result of our quasi-static analysis might be manipulated, which is not desirable. Hence, the goal is to determine the maximum loading rate (displacement) that has minimal effect on the numerical results. We conducted a sensitivity analysis in this regard, and found that 0.5 mm of downward displacement (i.e., 0.5 mm/s loading rate) of the central loading pin was the most appropriate amount for the implemented beam model.

For the segment models (see Fig. 7(b)), all DOFs in the TBM shield and adjacent concrete segments were fixed. A 2000-kN force, equivalent to a bearing pressure of 35 MPa, was applied over an area of 22×26 cm on the end surface of the segment (i.e., representing the hydraulic jack's contact area with the end of the segment), to analyze the effect of concentrated applied forces on the structural response of the segments. Additionally, misalignment (of up to 15°) between the direction of the TBM jack thrust force and the segment's longitudinal axis were investigated. Symmetric boundary conditions (XSYMM) were assumed to optimize computational efficiency.

For modelling the constitutive behavior of the C40-Class concrete, the concrete damage plasticity (CDP) model was chosen on account of its capability to simulate both compressive and tensile damage progression [59,60]. Fig. 8 illustrates the tension stiffening and compression hardening associated with the tensile and compressive responses.

The input parameters for the CDP model, as determined or deduced from the laboratory experiments performed in the present study, are listed in Table 3.

The model parameters include bulk density, elastic modulus, Poisson's ratio, yield stress σ_y, plastic strain ε_p, the biaxial yield stress to uniaxial yield stress ratio σ_{b0}/σ_{c0}, dilation angle $\psi(\theta.f_i)$, adjustment coefficient for $\psi(\theta.f_i)$ based on the hydrostatic stress (i.e., $\varepsilon(\theta.f_i)$), invariable ratio of tensile to compressive stresses (i.e., K_c), and damage coefficients in compression (d_c) and tension (d_t). With consideration of the experimental results, the initial values for the auxiliary parameters (i.e., σ_{b0}/σ_{c0}, $\psi(\theta.f_i)$, $\varepsilon(\theta.f_i)$, and K_c) of the CDP model were determined based on the reference manuals, related research articles [59,61], and ABAQUS documentation. The initial values of these parameters were then modified/adjusted accordingly through the verification process.

Moreover, the elastic–perfectly-plastic constitutive model was employed for the steel rebar and fiber reinforcements (refer to Table 4).

4. Results and discussion

4.1. Laboratory experiments

Table 5 and Fig. 9 present the laboratory test results for the unreinforced concrete (UC) specimens and five distinct FRC sample types (i.e., FRC1 to FRC5), characterized by their three different fiber diameters and contents investigated. Note the UC results serve as a control for gauging the fiber influence on the strength responses.

Referring to sample types FRC1, FRC2 and FRC3 containing 0.8 mm diameter fibers, the mobilized strengths increased overall for increasing the FC from 30 to 50 kg/m^3 (of the final concrete mix plan). The exception was the compressive strength mobilized for steel

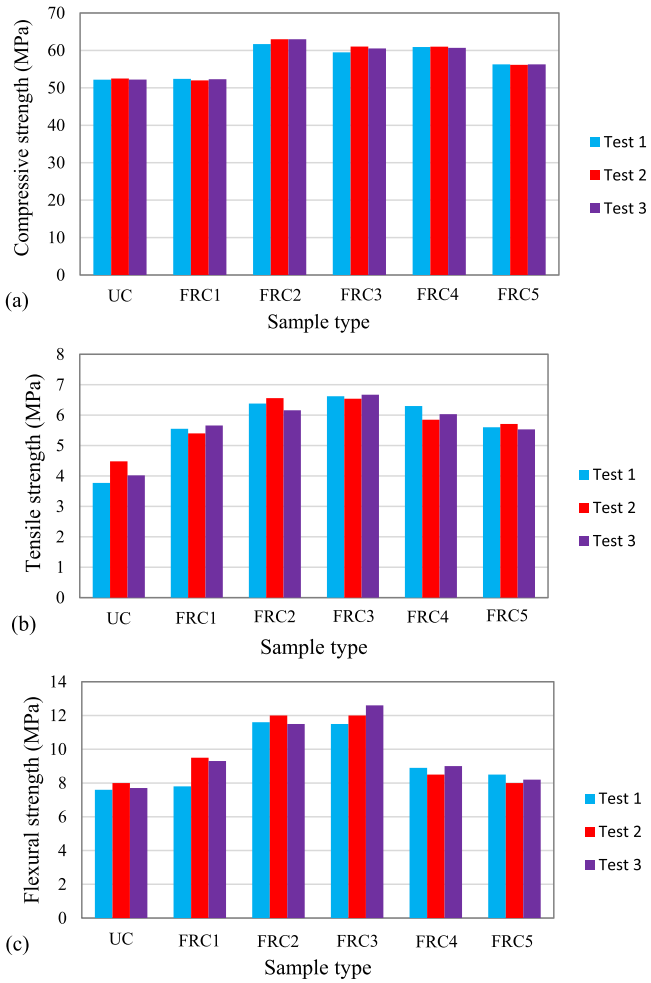

Fig. 9. Laboratory results for unreinforced concrete (UC) and FRC sample types: (a) compressive strength; (b) tensile (Brazilian) strength; (c) flexural strength. Refer to Table 5 for details of the steel fibers incorporated in the FRC samples.

fibers at 50 kg/m^3, which was slightly lower than that mobilized for 40 kg/m^3, this behavior being consistent with the findings reported in [62]. This compressive strength decrease may be attributed to slippage or movements between fibers for the higher FC. Notably, the additions of steel fibers at 30 and 40 kg/m^3 produced significant improvements of the tensile strength, with respective strength gains of about 35% and 56% achieved relative to the UC case. Considering each strength test, the greatest strength improvements achieved relative to the UC case were: (i) a 21% increase in compressive strength for steel fibers at 40 kg/m^3; (ii) a 62% increase in tensile strength for steel fibers at 50 kg/m^3; (iii) a 55% increase in flexural strength for steel fibers at 50 kg/m^3. These experimental findings are in general agreement with the results reported in [63,64] for indirect tension, [65,66] for flexural strength, and [67–70] for compressive strength testing.

Comparing the results for sample types FRC2, FRC4 and FRC5 shown in Fig. 9, it is evident that increasing the fiber diameter (from 0.8 to 1.2 mm) for the same fiber content (of 40 kg/m^3) causes a progressive reduction in the mobilized compressive, tensile and flexural strengths. Considering each strength test, relative to the 0.8 mm diameter fibers of the FRC2 case, the strength reductions for the FRC5 case employing 1.2 mm diameter fibers were a 62% decrease in compressive strength, 33% decrease in tensile strength, and an 88% decrease in flexural strength. However, it should be noted that in all investigated cases, the compressive, tensile and flexural strengths of the FRC samples were greater than those mobilized for the UC specimens. The strength reductions for increasing the fiber diameter (from 0.8 to 1.2 mm) with the same fiber content (of 40 kg/m^3) can be linked to the reducing number of individual fibers distributed throughout the test specimens for increasing fiber diameter. The number of individual fibers decreases by 54% (i.e., from 4830 to 2200 fibers per kilogram of steel fiber reinforcement: see Table 1) for increasing the fiber diameter from 0.8 to 1.2 mm. Consequently, for the larger diameter fibers, the number of interactions between the embedded fibers and concrete matrix decreases, leading to an overall weakening of the reinforced-concrete element.

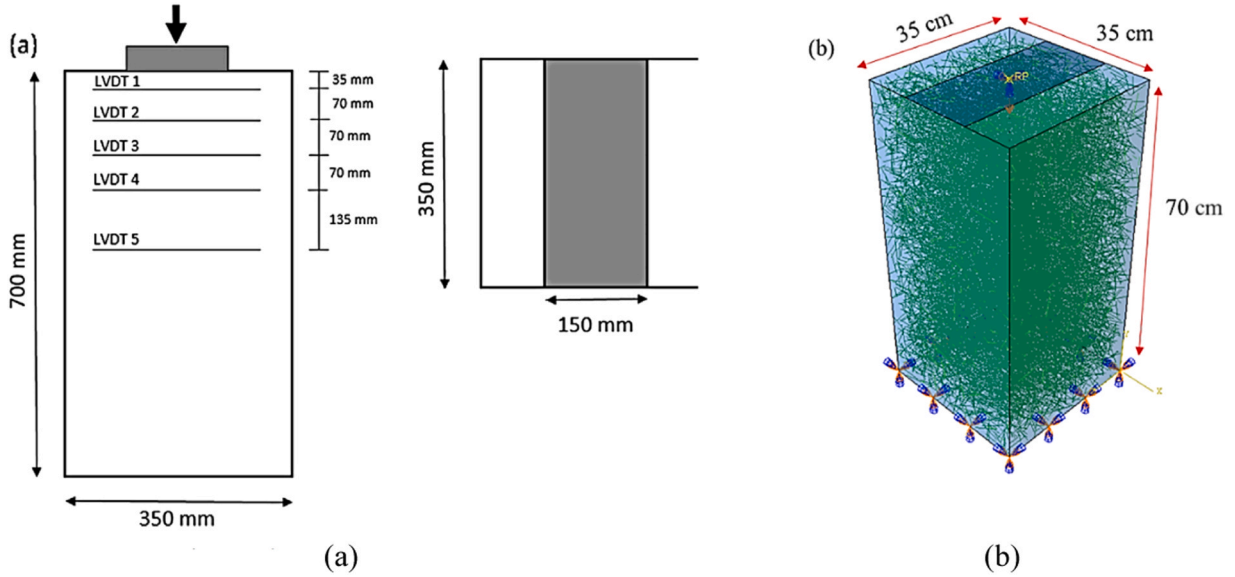

Fig. 10. Line-load compression test for FRC anchor block: (a) schematic elevation and plan views of the laboratory test setup [71]; (b) numerical model implemented in the present investigation.

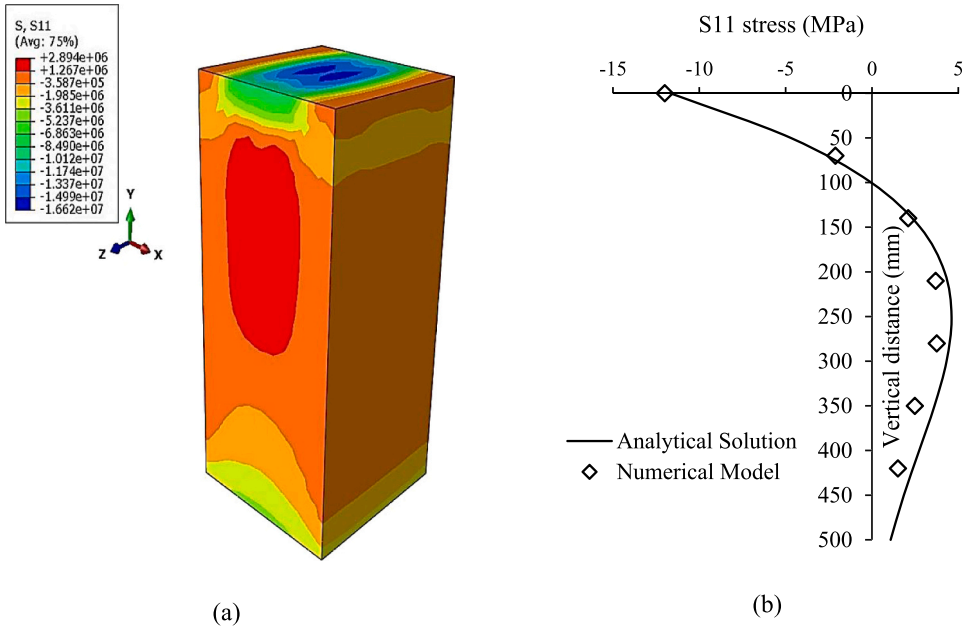

Fig. 11. Evolution of tensile (i.e., σ_{xx} or S11) stress for compressive force of 1150 kN applied to strip area (of 35×15 cm) centered on the 35-cm-square top surface of the FRC anchor block element: (a) numerical predictions in the present investigation; (b) comparison of our numerical results with the analytical solution proposed by [73].

4.2. Numerical analyses

This section begins with establishing the validity and accuracy of the employed numerical analyses by comparing the obtained numerical results with experimental data and established analytical solutions. Next, we present and analyze the numerical results obtained from RRC, FRC and FRRC beam model simulations that mirrored the loading conditions of the laboratory three-point bend test. Then, from comparisons of simulated RRC, FRC and FRRC segment types, we investigated the impact of including the fiber reinforcement on the structural performance/integrity of the segments for TBM jack loading.

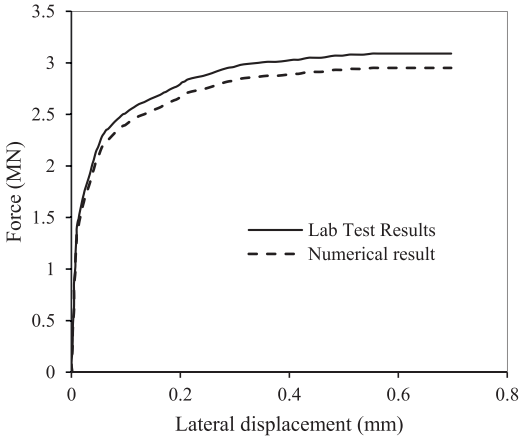

Fig. 12. Experimental vs. numerical results of axial force against lateral displacement for FRC anchor block (shown in Fig. 10a), considering the LVDT3 position for lateral displacement measurement (experimental data from [71]).

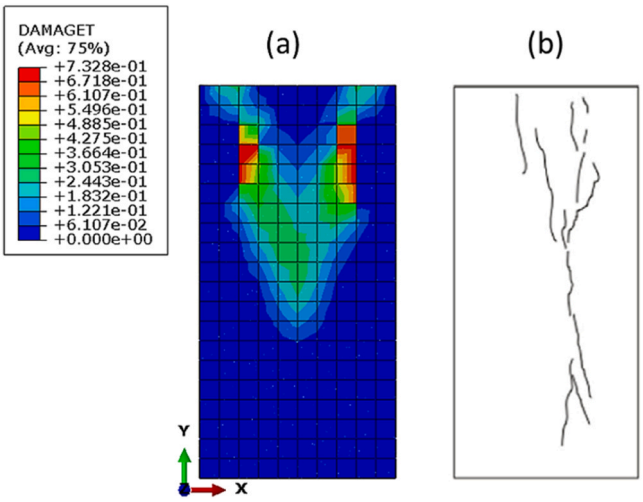

Fig. 13. Crack patterns for the investigated FRC anchor block: (a) simulation performed in present study (b) experimental [71].

4.2.1. Verification and validation of numerical analyses

For model verification and validation purposes, we compared the results of the employed numerical analysis to: (i) an experimental FRC anchor-block study reported in Schnüntger and Erdem [71] (which has also been used in [13,72] for validating their models); (ii) the analytical solution proposed by Zhou [73] for a concentrated compressive loading condition.

Schnüntger and Erdem [71] performed a series of line-load compression experiments on twelve 350-mm-square by 700 mm long FRC blocks (Fig. 10(a)). Comparable with the present investigation, their FRC mixes contained 35 kg of steel Dramix hooked-end fibers per cubic meter of the final concrete mix plan, each fiber being 0.75-mm in diameter by 60-mm long.

A 3D model was developed as part of the present study to replicate both the geometry and loading condition of the mentioned test setup. In other words, vertical displacement was constrained at the bottom surface (i.e., $u_y = 0$), while a displacement-controlled loading condition, with a magnitude of 2 mm/s, was applied to a strip area (of 35×15 cm) centered on the top surface of the anchor block element (see Fig. 10(b)). The resulting reaction force (i.e., macroscopic compressive strength) was monitored for each data output increment, with the maximum value of the reaction force equating to the predicted ultimate load capacity of the anchor block. Furthermore, the line-load configuration mobilizes tensile stress (i.e., splitting or bursting pressure, P_{sp}) orthogonal to the force direction (i.e., acting in the x direction for the model output shown in Fig. 11a), thereby providing insights into the two-dimensional biaxial behavior of the FRC element.

Before validating our numerical results for the anchor block model against the reported experimental results for the physical anchor block tested in Schnüntger and Erdem [71], we first verified our numerical results for loading in the elastic region, comparing them with the elastic analytical solution proposed by Zhou [73] for the concentrated compressive loading condition (see Fig. 11(b)). For this purpose, we considered the case of a 1150-kN compressive force applied to the 35×15-cm strip loading area on the top surface of the anchor block element (i.e., here the applied force is significantly below the element's ultimate load capacity of 3090 kN). As evident

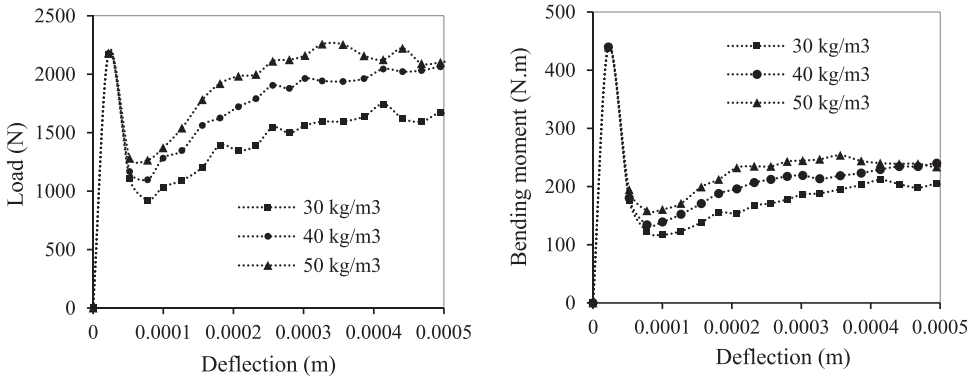

Fig. 14. Flexural load/bending moment against mid-span deflection results from FRC beam simulations, investigating 0.8-mm-diameter steel fibers at 30, 40, and 50 kg/m^3 (of the final concrete mix plan).

from the plot of tensile stress (i.e., σ_{xx} or S11) against measured distance vertically from the top of the anchor block (i.e., along its *y*-axis) shown in Fig. 11(b), our numerical model accurately replicates the FRC anchor block behavior in the pre-cracked (elastic) regime. In other words, the developed numerical models in this study faithfully reproduce the elastic stress distribution of FRC material under concentrated compressive loads, akin to the thrust force exerted by the TBM's hydraulic jack in the field scenario.

To evaluate the validity of our numerical model when considering the damage initiation and evolution in reinforced concrete, we compared the macroscopic compressive force predicted for the anchor block from the simulation with the experimental data reported in [71]. Overall, there was a good agreement achieved between the predicted macroscopic behavior and the experimental results for the FRC anchor block, with the maximum experimental load reaching 3.09 MN, while our numerical results showed a comparable maximum load of 2.98 MN (i.e., with 95.5% prediction accuracy)). To further validate the numerical results, we compared Schnütgen and Erdem [71]'s experimental and our numerical axial-force-against-lateral-displacement response/prediction for the LVDT3 position, i.e., for a distance of 175 mm down from the top end of the anchor block (see Fig. 10(a)). Fig. 12 illustrates the good agreement between the experimental and numerical results of axial force plotted against the LVDT3 (lateral) displacement.

Fig. 13 compares the simulated crack pattern with that observed during the FRC anchor block experiments reported in [71]. Initially, divergent tensile cracking occurred at the boundary (edge) of the 35×15-cm strip loading region, i.e., near the compressive/crush zone where direct contact occurs between the loading strip and anchor block. Moving down along the block length towards its mid-height, the induced maximum tensile stresses converge, producing a single/concentrated crack that is approximately aligned along the longitudinal axis of the block. The good agreement found between the numerically predicted and observed crack patterns is another key indication of the model's effectiveness in replicating the mechanical response of the FRC block element for the line-load configuration that ultimately leads to splitting/bursting failure. Moreover, the numerical model captured the intricate details of the crack initiation, propagation and interaction, thereby providing valuable insights into the resistance mechanism(s) of the FRC block until failure.

4.2.2. Beam model simulations

This section presents simulations for the 10-cm-square by 50-cm-long FRC, RRC, and FRRC beam elements, focusing on their mechanical behaviors, such as flexural load and bending moment resistances plotted against mid-span deflection, ultimate load capacity, and damage evolution. These serve as a basis for understanding the behaviors of the more complex FRRC segment element scenarios examined in the Section 4.2.3.

The first series of models investigated the flexural behavior of three FRC beams incorporating 0.8-mm-diameter steel fibers at 30, 40 and 50 kg/m^3 (of the final concrete mix plan) (see Fig. 14).

As per the studies by [28,74], three distinct stages are identified in the load–deflection behaviors of the FRC beams: (i) linear elastic; (ii) softening; (iii) fracture instability (expansion). During the softening stage, micro cracking develops continuously, causing a nonlinear load–deflection relationship. For the third stage, the fractures expand rapidly upon reaching the load capacity limits. The presence of the steel fibers hindered crack propagation, thereby contributing to an overall strengthening and toughening of the FRC beam elements.

As evident from Fig. 14, all three FRC beams exhibited similar load against mid-span deflection behaviors leading up to yield (i.e., first peak). However, their post-yield responses varied depending on the FC, i.e., with additions of steel fibers at 30 and 50 kg/m^3 producing the lowest and highest flexural strength capacities, respectively. The hardening response (post-yield) most likely arose due to the engagement and interaction between the embedded fibers and the concrete matrix. An evaluation of the localized cracking damage predicted in the middle section of the beams revealed less damage occurred for increasing FC. In other words, more engagements between the fibers and concrete matrix hindered the progress of micro-cracks.

The second series of models investigated the flexural behavior of three similarly dimensioned RRC beams, each incorporating 8, 10, or 12 mm diameter rebar. Limited by their small (i.e., 10×10 cm) cross-sectional area, two levels of rebars (wire meshes) were included in each beam: the lower wire mesh located in the tension zone, and the upper wire mesh located in the compression zone. This

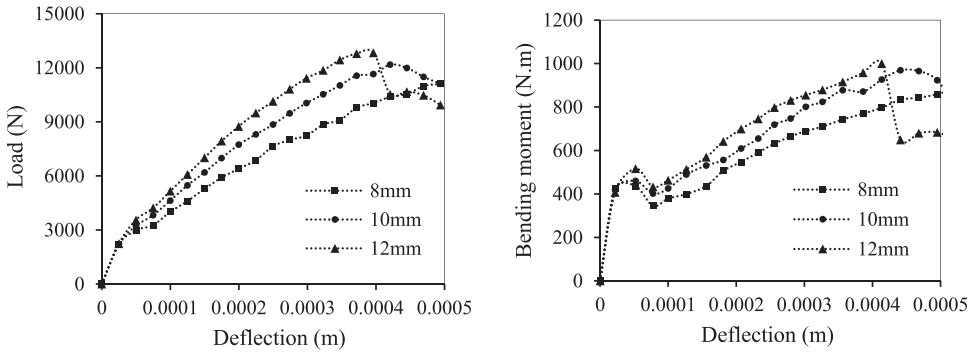

Fig. 15. Flexural load/bending moment against mid-span deflection results from RRC beam simulations (cases of four number of 8, 10, and 12 mm diameter rebars, i.e., two each in the tension and compression zones).

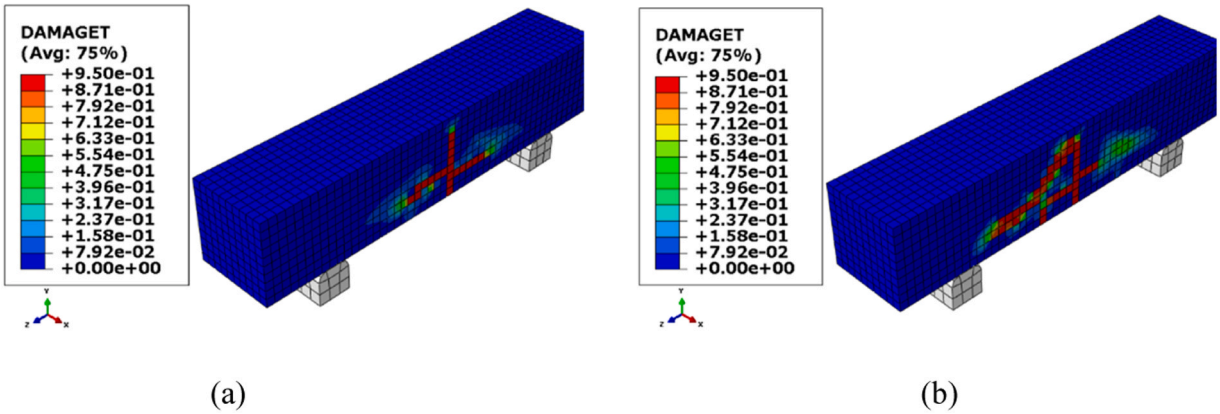

Fig. 16. Damage progression predicted in the RRC beams for (a) 8 mm and (b) 12 mm diameter rebars.

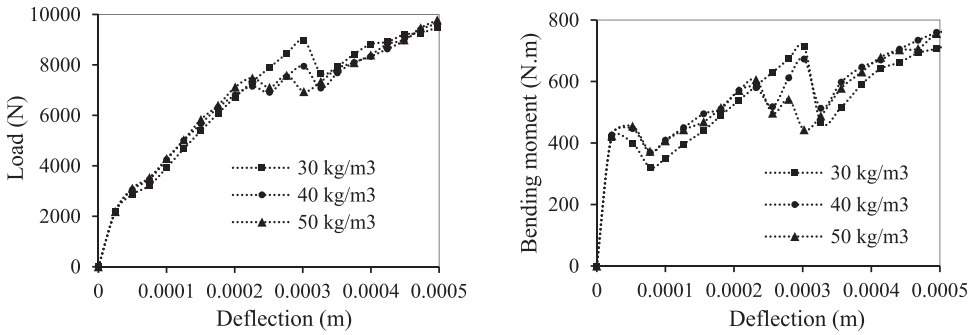

Fig. 17. Flexural load/bending moment against mid-span deflection results from FRRC beam simulations (case of two 8-mm-diameter rebars and 0.8 mm diameter fibers, considering FCs of 30, 40, and 50 kg/m^3 (of the final concrete mix plan)).

configuration entails incorporating two rebars within each wire layer, i.e., giving four rebars foreach beam. The four rebars were spaced at 4-cm centers (in the *x* and *y* directions; see Fig. 7(a)), with a 3 cm concrete cover to each rebar. Elongation of the rebars occurred along the *z*-axis under the imposed flexural loading. Referring to the simulation results shown in Fig. 15, all three RRC beams behaved identically up to the yield point. However, as expected, their post-yield hardening responses differed, with greater flexural strength mobilized for larger diameter rebar. Moreover, the ultimate flexural strengths mobilized for the RRC beams were more than five times greater than those mobilized by the FRC beams.

Fig. 16 shows the damage predicted for the RRC beams incorporating 8 and 12 mm diameter rebars, with more extensive damage to the beam occurring for the larger diameter rebar. This is attributed to the higher rigidity and energy absorption of the larger diameter rebar, which makes the adjacent concrete more susceptible to damage. In other words, the rebars primarily enhanced the flexural strength capacity of the beam elements rather than the structural integrity of the concrete, which experienced extensive damage

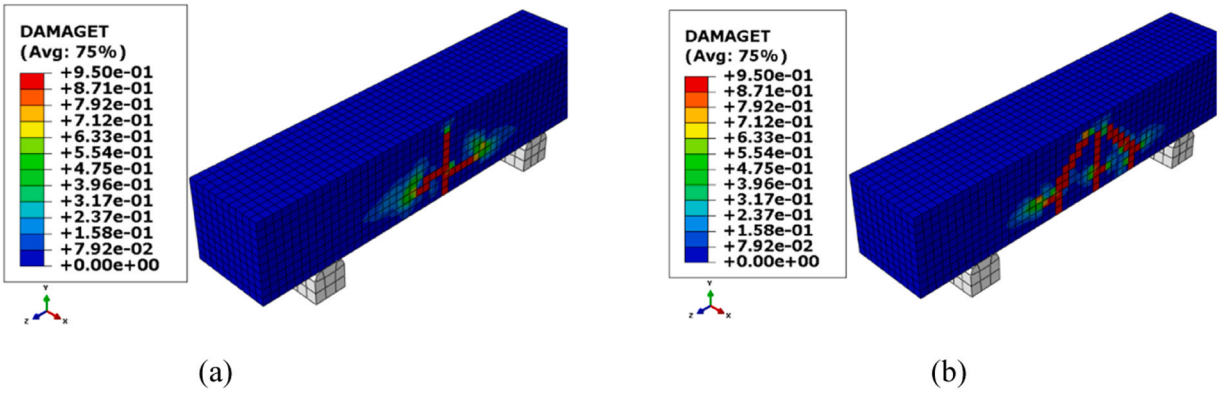

Fig. 18. Damage progression in the FRRC beams incorporating two number of 8-mm diameter rebars and 0.8 mm diameter fibers, considering (a) 30 kg/m^3 and (b) 50 kg/m^3 (of the final concrete mix plan).

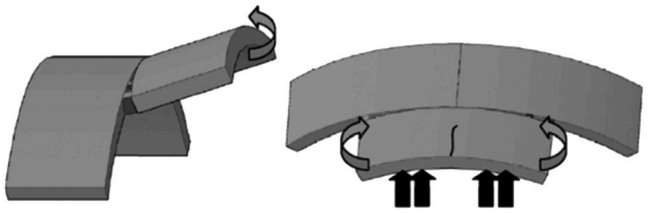

Fig. 19. Schematic of improper ring contact caused by misalignment of the TBM jacks with the longitudinal axis of the tunnel lining [50].

Table 6
Threshold pressure causing damage to differently reinforced segment types, considering misalignment of the TBM jack thrust force with the longitudinal axis of the already installed tunnel lining.

		Damage threshold pressure (in MPa) for jack misalignments of:			
Segment type	Quantity of reinforcement	0°	7.5°	10°	15°
RRC	12 no. of main rebars (each 10 mm dia.), and 36 no. of shear rebars (each 8 mm dia.)	29.8	26.3	17.5	5.3
FRC	30 kg/m^3 of 0.8-mm dia. steel fibers	>35	33.3	21.0	7.0
FRC	40 kg/m^3 of 0.8-mm dia. steel fibers	>35	31.5	19.5	5.3
FRC	50 kg/m^3 of 0.8-mm dia. steel fibers	>35	33.3	21.0	7.0
FRRC	12 no. of main rebars (each 8 mm dia.), and 0.8 mm dia. steel fibers at 40 kg/m^3	>35	33.3	19.5	7.0

progression.

The third series of models investigated the flexural behavior of three FRRC beams having the same dimensions (i.e., 10-cm-square by 50-cm long) as the first and second series of models. The reinforcement designs for the FRRC beams were based on the 0.8-mm-dia. fiber consumption requirement of 30, 40 and 50 kg of steel fibers per cubic meter of concrete, along with a lower wire mesh containing two 8-mm-dia. rebars. In other words, the two rebars were spaced at 4-cm centers (in the *x* direction; see Fig. 7(a)), with a 3 cm concrete cover between them and the beam's bottom surface. Fig. 17 presents the flexural load/bending moment against mid-span deflection results obtained from the three FRRC beam simulations.

Referring to Figs. 15 and 17, the flexural strength capacities of the three FRRC beams and the RRC beam with 8-mm-dia. rebars were approximately equal. In other words, the flexural strength capacity of the FRRC beams was controlled mostly by the rebars, and not the fiber reinforcement. Referring to Fig. 18, greater damage of the FRRC beams occurred for the higher FC (of 50 kg/m^3). This is explained by more contacts between the steel fibers and the rebars for higher FC, resulting in more slippage/movement occurring between them, thereby contributing to the formation and development of more severe damage in the concrete.

4.2.3. Structural performance of CWCT segmented lining during installation phase

Using numerical modelling, this section investigates the effect of a concentrated force, applied by the TBM jack during the lining's installation phase, on the stress distribution, deformation patterns, and damage evolution for the RCC, FRC, and FRRC segment types. The magnitude of the applied jack force depends on many variables, including the ground conditions, tunnel overburden, friction forces developed between the TBM shield and surrounding soil, the number of hydraulic jacks employed per segment, the loading plate's contact area, etc. It is also worth noting that the most demanding scenarios for loads and concrete cracking may not occur

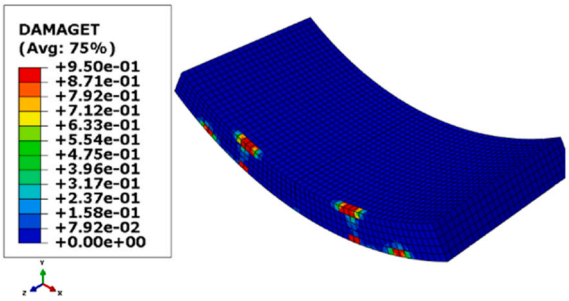

(a) Perfectly aligned RRC segment.

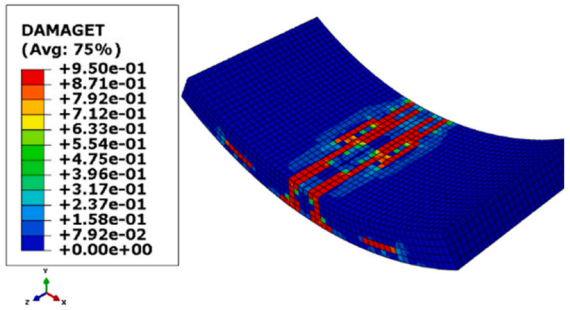

(b) RRC segment with 15° jack misalignment.

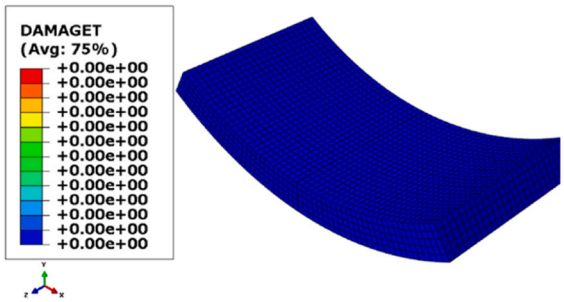

(c) Perfectly aligned FRC segment.

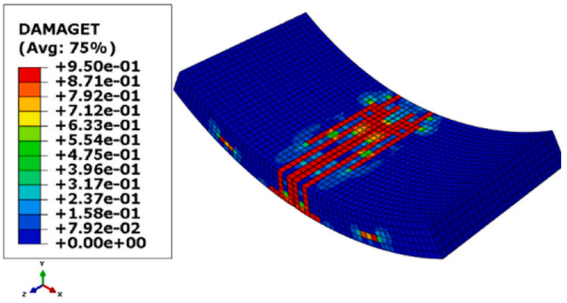

(d) FRC segment with 15° jack misalignment.

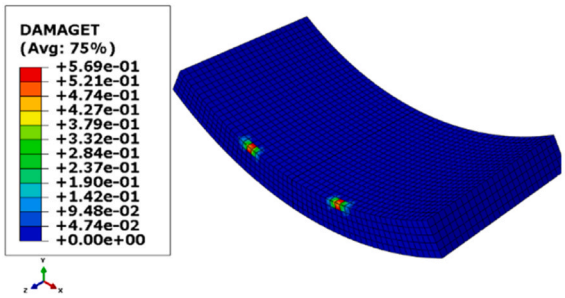

(e) Perfectly aligned FRRC segment.

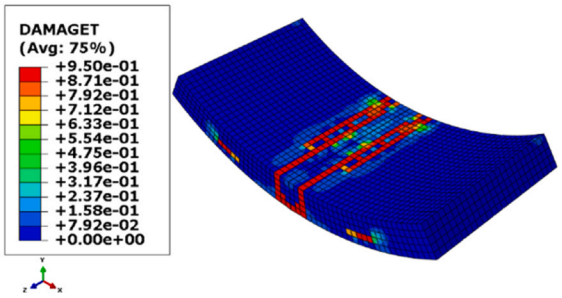

(f) FRRC with 15° jack misalignment.

Fig. 20. Damage predictions for RRC, FRC, and FRRC segment types, investigating the cases of the hydraulic jack thrust applied in (a, c, e) perfect alignment and (b, d, f) at a 15° misalignment with the longitudinal axis of the already installed tunnel lining.

during the tunnel construction stage [5,75]. Furthermore, imperfect segment placement, jack misalignment, or operator error can result in improper ring contact (see Fig. 19) and load eccentricity [13,76].

For our numerical simulations, the models considered perfect alignment (i.e., 0°) and misalignments of 5°, 7.5°, 10°, and 15° between the TBM thrust direction and the longitudinal axis of the already installed tunnel lining. The segment model shown in Fig. 7(b) was employed, investigating C40-Class concrete with the following reinforcement schemes (see also Table 6):

- RRC segment incorporating 10-mm-diameter main reinforcement (i.e., 12 rebars in two layers, 6 rebars each), along with 8-mm-diameter shear reinforcement (36 rebars in two layers).
- Three FRC segments incorporating 0.8-mm-diameter steel fibers at 30, 40, and 50 kg/m^3 (of the final concrete mix plan).

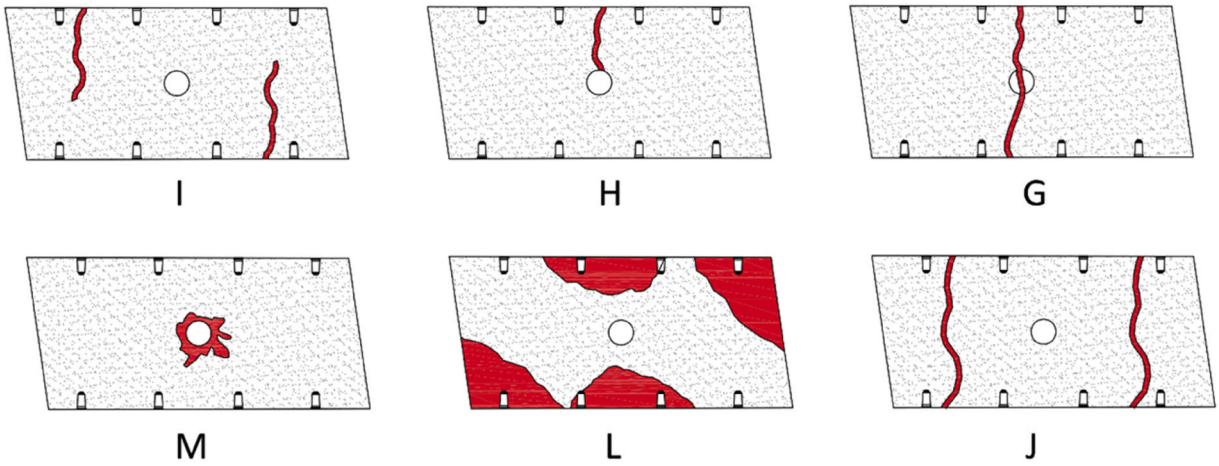

Fig. 21. Visual classification of six distinct damage patterns identified on the inner faces of individual segments comprising the in-situ CWCT lining (patterns are labelled G, H, I, J, L, and M).

- FRRC segment incorporating 8-mm-diameter main reinforcement (12 rebars arranged in two layers, 6 rebars each), along with 0.8-mm-diameter steel fibers at 40 kg/m^3 (of the final concrete mix plan).

Note, the RRC and FRC reinforcement schemes described above are the same as those used in fabricating the RRC and FRC segment types utilized in the actual CWCT lining. The additional analysis for the FRRC segment type serves to explore reinforcement variations, i.e., different from the field reinforcement plan design.

Fig. 20 presents the results from the RRC, FRC and FRRC simulations, considering the cases of the single hydraulic jack in (i) perfect alignment, and (ii) at a 15° misalignment with the longitudinal axis of the already installed tunnel lining. In the case of their perfect alignment (Fig. 20(a, c, e)), no significant damage was predicted for both the FRC and FRRC segment types, whereas considerable damage occurred for the RRC segments in the vicinity of the applied TBM jack force (refer to Fig. 7(b) for locating the jack thrust force applied to the end area of the segment. This failure/damage mechanism is quite similar to the formation of a crushing zone under the TBM roller disc-cutter, from which tensile fractures can develop. As demonstrated for flexure loading of the model beams in Section 4.2.2, the rebars in the RRC segments merely enhanced the beam's structural strength capacity, whereas the addition of fibers helped to improve the overall mechanical behavior of the reinforced-concrete elements, reducing their tendency for chipping damage formation.

Fig. 20(b, d, f) show the numerical predictions for the case of the jack thrust force applied at a 15° misalignment with the longitudinal axis of the already installed tunnel lining. Regardless of the reinforcement scheme employed, even modest jack misalignments (of 5–7.5°) resulted in the segments experiencing some damage, mostly occurring in the middle section where transverse cracks formed. Table 6 lists the predicted threshold pressure magnitudes above which the segments sustained damage. As expected, increased jack misalignment caused the segments to experience damage for lower jack thrust force, with the threshold damage pressure decreasing proportionately.

5. Statistical study of observed damage patterns in CWCT lining segments

A field-monitoring program of the installed CWCT lining was performed, involving detailed observations for a total of 961 segments (comprising 545 RRC and 416 FRC) that had become damaged during their installation and in-service phases. The field observations served to document and quantify common damage patterns, with consideration of the six segment locations around (comprising) the lining ring (refer to Fig. 3). Statistical analysis of the collected data provided valuable insights into the performances of the RRC and FRC segment types under their operational conditions, and for comparison with the numerical simulation results. Fig. 21 categorizes into six distinct patterns the observed damages that had occurred to the 961 segments of the CWCT lining.

Fig. 22 presents the frequency of each damage pattern (as a percentage of the 545 RRC and 416 FRC damaged segments examined), with consideration also of their occurrence in the six segment locations comprising the lining ring (i.e., segments labeled A–E and K illustrated Fig. 3).

Referring to Fig. 22, the most frequent damage patterns observed on-site for both the C40-Class RRC and FRC segments were types G, J, and L. Referring to Fig. 21, patterns G and J are related to cracking damage across the entire segment width, while pattern L is associated with chipping damage in the segment corners and along longitudinal/circumferential joints. As observed in the frequency charts of Fig. 22, the FRC segments were notably less susceptible to chipping damage (pattern L) than the RRC segments. However, approximately 70% and 50% of the damaged RRC and FRC segments, respectively, experienced cracking damage (patterns G and J). As observed for the segment models, cracking damage likely occurred due to the concentrated force action arising from the hydraulic jack's misalignment with the longitudinal axis of the already installed tunnel lining, which caused crack formation regardless of the

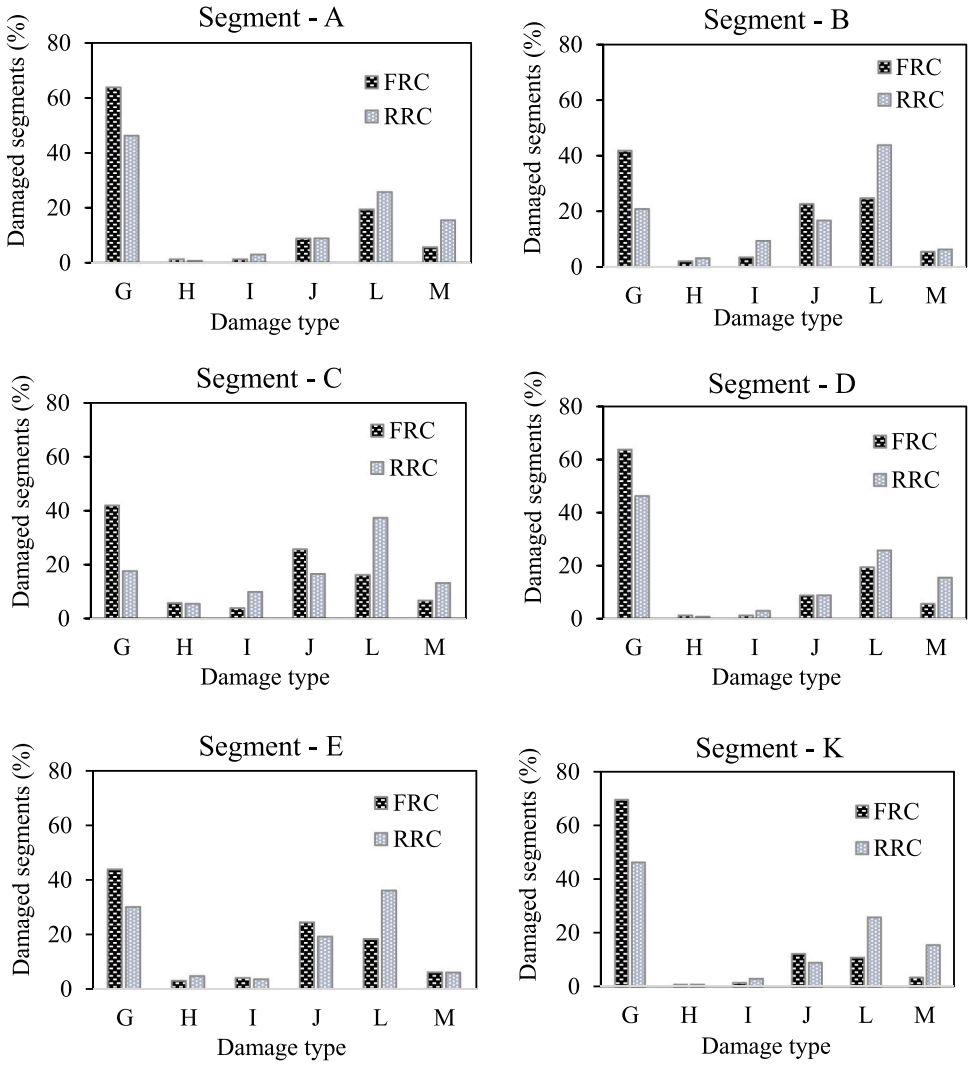

Fig. 22. Analysis of 961 damaged segments, considering the six distinct damage patterns identified from inspection of the CWCT lining. [Refer to Fig. 21 for illustrations of the damage patterns labelled G, H, I, J, L, and M. Refer to Fig. 3 for the locations of the six individual segments (labelled A–E, and K) that comprise the lining. Data set comprised 545 RRC and 416 FRC segments].

segment reinforcement scheme adopted.

6. Summary and conclusions

Employing a combination of laboratory experiments, numerical modeling, and statistical analysis of field performance data, this paper presented a comprehensive evaluation of the efficacy of incorporating rebar and steel fiber reinforcement in the C40-Class precast concrete segments that comprise the lining of the Chamshir water conveyance tunnel (CWCT). The laboratory experiments revealed that for steel fiber-reinforced concrete (FRC) elements, an increase in fiber content or reduction in fiber diameter (for investigated ranges of 30–50 kg/m^3 (of the final concrete mix plan) and 0.8–1.2 mm, respectively) produced improvements in compressive, tensile, and flexural strengths. Notably, for these FRC elements, the tensile (i.e., Brazilian) strength exhibited the most significant improvement, whereas the enhancement in compressive strength was comparatively modest.

Numerical simulations of three-point load tests on similar dimensioned rebar-reinforced concrete (RRC), FRC, and steel fiber-rebar-reinforced concrete (FRRC) beam models demonstrated that, in terms of ultimate flexural strength, the RRC and FRRC beams achieved comparable performance, whereas the FRC beams exhibited significantly lower ultimate flexural strength, albeit that they showed reduced localized cracking damage compared to their counterparts. In other words, the flexural strength capacity of the FRRC beams was controlled mostly by the rebars (and not the fiber reinforcement), whereas the structural integrity performances of the FRC and FRRC beams was superior because of the fiber reinforcement.

Simulations of RRC, FRC, and FRRC segment types subjected to concentrated force (applied by the hydraulic jack during

installation of the CWCT lining) indicated minimal damage would occur for the FRC and FRRC segment types, whereas the RRC segments were predicted to sustain considerable damage. In other words, the fiber reinforcement not only enhanced structural strength capacity, but also mitigated the formation of chipping damage, including for modest jack thrust misalignment.

Statistical analysis of 961 damaged segments of the CWCT lining highlighted the susceptibility of both RRC and FRC segment types to cracking and chipping damages. This mostly arose due to the concentrated force action in response to the jack misalignment with the longitudinal axis of the already installed tunnel lining. However, compared to the RRC segments, the FRC segments exhibited notably lower susceptibility to chipping damage regardless of the jack thrust misalignment.

In conclusion, this study provides valuable insights into the mechanical behaviors, strengths, and vulnerabilities of FRC segments used in tunnel construction. Additionally, the integration of fiber reinforcement with conventional rebar offers a promising approach to achieve enhanced concrete performance and mitigate damage to tunnel segmented linings, with broad potential applications in various infrastructure projects.

Funding

This research did not receive any specific grant from funding agencies in the public, commercial, or not-for-profit sectors.

CRediT authorship contribution statement

Mohammad Farouq Hossaini: Writing – original draft, Validation, Supervision, Data curation, Conceptualization. **Rasoul Sheikhmall:** Writing – review & editing, Visualization, Methodology, Formal analysis. **Mohammad Ezazi:** Writing – original draft, Visualization, Validation, Methodology, Investigation, Formal analysis, Data curation, Conceptualization. **Ebrahim Sharifi Teshnizi:** Writing – review & editing, Formal analysis. **Brendan C. O′Kelly:** Writing – review & editing, Visualization, Validation. **Mohammad Khosrotash:** Methodology, Conceptualization.

Declaration of Competing Interest

The authors declare that they have no known competing financial interests or personal relationships that could have appeared to influence the work reported in this paper.

Data availability

Data will be made available on request.

References

[1] S. Feng, Z. Chen, H. Luo, S. Wang, Y. Zhao, L. Liu, D. Ling, L. Jing, Tunnel boring machines (TBM) performance prediction: a case study using big data and deep learning, Tunn. Undergr. Sp. Technol. *110* (2021) 103636, https://doi.org/10.1016/j.tust.2020.103636.
[2] A. Meda, Z. Rinaldi, S. Spagnuolo, B. de Rivaz, N. Giamundo, Hybrid precast tunnel segments in fiber reinforced concrete with glass fiber reinforced bars, Tunn. Undergr. Sp. Technol. *86* (2019) 100–112, https://doi.org/10.1016/j.tust.2019.01.016.
[3] F. Gruebl, Segmental rings (critical loads and damage prevention), *Proc. Int. Symp. Undergr. Excav. Tunn., Bangk., Thail.* (2006) 9–19.
[4] Q. Ai, Y. Gu, Y. Yuan, X. Jiang, H. Wang, H. Yu, Y. Huang, Integrated waterproofing evaluation method for longitudinal joints of shield tunnel subjected to extreme surcharge: numerical analysis and experimental validation, Tunn. Undergr. Sp. Technol. *131* (2023) 104834, https://doi.org/10.1016/j.tust.2022.104834.
[5] M. Sugimoto, Causes of shield segment damages during construction: *Proc. Int. Symp. Undergr. Excav. Tunn., Bangk., Thail.* (2006) 67–74.
[6] S.H.P. Cavalaro, C.B.M. Blom, J.C. Walraven, A. Aguado, Structural analysis of contact deficiencies in segmented lining, Tunn. Undergr. Sp. Technol. *26* (2011) 734–749, https://doi.org/10.1016/j.tust.2011.05.004.
[7] E. Gholami, H. Afshin, M. Charkhtab Basim, M. Sharghi, Ultra-high performance recycled steel fiber reinforced concrete segments under the thrust force of TBM jacks and their environmental potentialities, Structures *47* (2023) 2465–2484, https://doi.org/10.1016/j.istruc.2022.12.051.
[8] C.B.M. Blom, Design philosophy of concrete linings for tunnels in soft soils. PhD thesis, Delft University of Technology, Delft, The Netherlands, 2002.
[9] M. Herrenknecht, K. Bäppler, Segmental concrete lining design and installation, *Proc. Soft Ground Hard Rock. Mech. Tunn. Technol. Semin.* (2003).
[10] A. Caratelli, A. Meda, Z. Rinaldi, Design according to MC2010 of a fibre-reinforced concrete tunnel in Monte Lirio, Panama, Struct. Concr. *13* (2012) 166–173, https://doi.org/10.1002/suco.201100034.
[11] H. Hu, T. Xue, J. Li, P. Liu, B. Wang, Y. Liu, Mechanical performance of concrete segment lining structure of shield tunneling in different strata, Buildings *13* (2023) 3118, https://doi.org/10.3390/buildings13123118.
[12] J. Xia, Flexural behavior of high-strength steel and ultra-high-performance fiber-reinforced concrete composite beams, Buildings *14* (2024) 131, https://doi.org/10.3390/buildings14010131.
[13] R. Burgers, Non-linear FEM modelling of steel fibre reinforced concrete (for the analysis of tunnel segments in the thrust jack phase), Delft University of Technology, The Netherlands, 2006.
[14] D. Cui, L. Wang, C. Zhang, H. Xue, D. Gao, F. Chen, Dynamic splitting performance and energy dissipation of fiber-reinforced concrete under impact loading, Materials *17* (2024) 421, https://doi.org/10.3390/ma17020421.
[15] J.D. Ortiz, S.S.K. Dolati, P. Malla, A. Mehrabi, A. Nanni, Nondestructive testing (NDT) for damage detection in concrete elements with externally bonded fiber-reinforced polymer, Buildings *14* (2024) 246, https://doi.org/10.3390/buildings14010246.
[16] A. Caratelli, A. Meda, Z. Rinaldi, P. Romualdi, Structural behaviour of precast tunnel segments in fiber reinforced concrete, Tunn. Undergr. Sp. Technol. *26* (2011) 284–291, https://doi.org/10.1016/j.tust.2010.10.003.
[17] A. de la Fuente, A. Aguado, C. Molins, J. Armengou, Innovations on components and testing for precast panels to be used in reinforced earth retaining walls, Constr. Build. Mater. *25* (2011) 2198–2205, https://doi.org/10.1016/j.conbuildmat.2010.11.003.
[18] E. Sharifi Teshnizi, J. Karimiazar, J.A. Baldovino, Effect of acid and thermo-mechanical attacks on compressive strength of geopolymer mortar with different eco-friendly materials, Sustain *15* (2023), https://doi.org/10.3390/su151914407.

[19] M. di Prisco, F. Iorio, G. Plizzari, HPSFRC prestressed roof elements, *Proc. Int. RILEM Workshop Test. Des. Methods Steel Fibre Reinf. Concr. — Backgr. Exp., Boch., Ger.* (2003) 161–188.

[20] T. Kasper, C. Edvardsen, G. Wittneben, D. Neumann, Lining design for the district heating tunnel in Copenhagen with steel fibre reinforced concrete segments, Tunn. Undergr. Sp. Technol. *23* (2008) 574–587, https://doi.org/10.1016/j.tust.2007.11.001.

[21] G.A. Plizzari, L. Cominoli, Numerical simulations of SFRC precast tunnel segments, *Proc. Int. World Tunn. Congr. 31st ITA Gen. Assem., Istanb., Turk.* Volume 2 (2005) 1105–1112.

[22] J.C. Walraven, High performance fiber reinforced concrete: progress in knowledge and design codes, Mater. Struct. *42* (2009) 1247–1260, https://doi.org/10.1617/s11527-009-9538-3.

[23] A. de la Fuente, P. Pujadas, A. Blanco, A. Aguado, Experiences in Barcelona with the use of fibres in segmental linings, Tunn. Undergr. Sp. Technol. *27* (2012) 60–71, https://doi.org/10.1016/j.tust.2011.07.001.

[24] L. Liao, A. de la Fuente, S. Cavalaro, A. Aguado, Design of FRC tunnel segments considering the ductility requirements of the Model Code 2010, Tunn. Undergr. Sp. Technol. *47* (2015) 200–210, https://doi.org/10.1016/j.tust.2015.01.006.

[25] S. Coccia, A. Meda, Z. Rinaldi, On shear verification according to *fib* Model Code 2010 in FRC elements without traditional reinforcement, Struct. Concr. *16* (2015) 518–523, https://doi.org/10.1002/suco.201400026.

[26] F. Di Carlo, A. Meda, Z. Rinaldi, Design procedure for precast fibre-reinforced concrete segments in tunnel lining construction, Struct. Concr. *17* (2016) 747–759, https://doi.org/10.1002/suco.201500194.

[27] B. Chiaia, A.P. Fantilli, P. Vallini, Combining fiber-reinforced concrete with traditional reinforcement in tunnel linings, Eng. Struct. (*31*) (2009) 1600–1606, https://doi.org/10.1016/j.cscm.2022.e01401.

[28] C. Yixin, Z. Jianye, M. Jicheng, Z. Shunli, L. Yongsheng, Z. Zhixuan, Tensile strength and fracture toughness of steel fiber reinforced concrete measured from small notched beams, Case Stud. Constr. Mater. *17* (2022) e01401, https://doi.org/10.1016/j.cscm.2022.e01401.

[29] J. Sridhar, R. Gobinath, M.S. Kırgız, Evaluation of artificial neural network predicted mechanical properties of jute and bamboo fiber reinforced concrete along with silica fume, J. Nat. Fibers *20* (2023) 2162186, https://doi.org/10.1080/15440478.2022.2162186.

[30] A. Karimi Pour, A. Shirkhani, J.J. Zeng, Y. Zhuge, E.N. Farsangi, Influence of fiber type on the performance of reinforced concrete beams made of waste aggregates: experimental, numerical, and cost analyses, Pract. Period. Struct. Des. Constr. *28* (2023) 4023007, https://doi.org/10.1061/PPSCFX.SCENG-1219.

[31] N. Bheel, M.O.A. Ali, M.S. Kırgız, N. Shafiq, R. Gobinath, Effect of graphene oxide particle as nanomaterial in the production of engineered cementitious composites including superplasticizer, fly ash, and polyvinyl alcohol fiber, Mater. Today Proc. (2023), https://doi.org/10.1016/j.matpr.2023.03.010.

[32] H.Y.B. Katman, W.J. Khai, N. Bheel, M.S. Kırgız, A. Kumar, O. Benjeddou, Fabrication and characterization of cement-based hybrid concrete containing coir fiber for advancing concrete construction, Buildings *12* (2022), https://doi.org/10.3390/buildings12091450.

[33] V. Mahesh, R. Gobinath, M.S. Kırgız, R.P.V. Shekar, M. Shewale, Global trends of research productivity in natural fibre reinforced composites: comprehensive scientometric analysis, J. Nat. Fibers *19* (2022) 13088–13105, https://doi.org/10.1080/15440478.2022.2085227.

[34] J. Sridhar, R. Gobinath, M.S. Kırgız, Comparative study for efficacy of chemically treated jute fiber and bamboo fiber on the properties of reinforced concrete beams, J. Nat. Fibers *19* (2022) 12224–12234, https://doi.org/10.1080/15440478.2022.2054894.

[35] A.M. Brandt, Fibre reinforced cement-based (FRC) composites after over 40 years of development in building and civil engineering, Compos. Struct. *86* (2008) 3–9, https://doi.org/10.1016/j.compstruct.2008.03.006.

[36] C. Jiang, K. Fan, F. Wu, D. Chen, Experimental study on the mechanical properties and microstructure of chopped basalt fibre reinforced concrete, Mater. Des. *58* (2014) 187–193, https://doi.org/10.1016/j.matdes.2014.01.056.

[37] K. Yu, L. Li, J. Yu, Y. Wang, J. Ye, Q.F. Xu, Direct tensile properties of engineered cementitious composites: a review, Constr. Build. Mater. *165* (2018) 346–362, https://doi.org/10.1016/j.conbuildmat.2017.12.124.

[38] L. Hou, R. Xu, Y. Zang, F. Ouyang, D. Chen, L. Zhong, Bond behavior between reinforcement and ultra-high toughness cementitious composite in flexural members, Eng. Struct. *210* (2020) 110357, https://doi.org/10.1016/j.engstruct.2020.110357.

[39] R.M. Waqas, A. Elahi, M.S. Kirgiz, N. Nagaprasad, K. Ramaswamy, Maintenance of crack with infilling polymer modified mortar for shear deficient of reinforced concrete beam, Sci. Rep. *14* (2024) 358, https://doi.org/10.1038/s41598-023-50519-0.

[40] J. Zhao, Y. Zhang, Y. Qin, Numerical and experimental studies on crack resistance of ultra-high-performance concrete decorative panels for bridges, Appl. Sci. *14* (2024) 636, https://doi.org/10.3390/app14020636.

[41] S. Wang, A. Madan, C. Zhao, E. Seong Huang, T. Su, B.J. Chiew, Y. Yang, Experimental study on strain of SFRC tunnel lining segments using a comprehensive embedded optical fiber sensing system, Measurement *223* (2023) 113791, https://doi.org/10.1016/j.measurement.2023.113791.

[42] X. Zhao, K. Han, J.W. Ju, X. Chen, W. Chen, H. Xiong, Numerical analysis of size effect on the deformation behavior and damage evolution mechanism of segmental tunnel lining rings, Int. J. Damage Mech. *32* (2023) 600–622, https://doi.org/10.1177/10567895231157436.

[43] H. Li, Y. Wu, A. Zhou, F. Lu, Z. Lei, B. Zeng, K. Zhu, Cracking pattern and bearing capacity of steel fiber-reinforced concrete single-layer tunnel lining, Sustain *15* (2023), https://doi.org/10.3390/su151310665.

[44] L. Sorelli, F. Toutlemonde, On the design of steel fiber reinforced concrete tunnel lining segments, *Proc. 11th Int. Conf. Fract., Turin, Italy,* volume 8 (2005) 5702–5707.

[45] R. Breitenbücher, G. Meschke, F. Song, M. Hofmann, Y. Zhan, Experimental and numerical study on the load-bearing behavior of steel fiber reinforced concrete for precast tunnel lining segments under concentrated loads, *Proc. FRC 2014 Jt. Acids-fib Int. Workshop — Fibre Reinf. Concr.: Des. Struct. Appl., Montr., Can.* (2014) 417–429.

[46] S. Abbas, A. Soliman, M. Nehdi, Structural behaviour of ultra-high performance fibre reinforced concrete tunnel lining segments, *Proc. FRC 2014 Jt. Acids-fib Int. Workshop — Fibre Reinf. Concr.: Des. Struct. Appl., Montr., Can.* (2014) 532–543.

[47] G. Tiberti, G. Plizzari, Final concrete linings with optimized reinforcement, *Proc. World Tunn. Congr. 2008 — Undergr. Facil. Better Environ. Saf., Agra, India,* volume 2 (2008) 922–932.

[48] M. Jamshidi Avanaki, A. Hoseini, S. Vahdani, A. de la Fuente, Numerical-aided design of fiber reinforced concrete tunnel segment joints subjected to seismic loads, Constr. Build. Mater. *170* (2018) 40–54, https://doi.org/10.1016/j.conbuildmat.2018.02.219.

[49] M. Jamshidi Avanaki, A. Hoseini, S. Vahdani, C. de Santos, A. de la Fuente, Seismic fragility curves for vulnerability assessment of steel fiber reinforced concrete segmental tunnel linings, Tunn. Undergr. Sp. Technol. *78* (2018) 259–274, https://doi.org/10.1016/j.tust.2018.04.032.

[50] G. Tiberti, E. Chiriotti, G. Plizzari, Twenty Years of FRC Tunnel Segments Practice: Lessons Learnt and Proposed Design Principles, International Tunnelling Association, 2016.

[51] T.L. Teng, Y.A. Chu, F.A. Chang, B.C. Shen, D.S. Cheng, Development and validation of numerical model of steel fiber reinforced concrete for high-velocity impact, Comput. Mater. Sci. *42* (2008) 90–99, https://doi.org/10.1016/j.commatsci.2007.06.013.

[52] O. Arnau, C. Molins, Experimental and analytical study of the structural response of segmental tunnel linings based on an in situ loading test. Part 2: Numerical simulation, Tunn. Undergr. Sp. Technol. *26* (2011) 778–788, https://doi.org/10.1016/j.tust.2011.04.005.

[53] D. Chen, X. Yu, R. Liu, S. Li, Y. Zhang, Triaxial mechanical behavior of early age concrete: experimental and modelling research, Cem. Concr. Res. *115* (2019) 433–444, https://doi.org/10.1016/j.cemconres.2018.09.013.

[54] M. Sharghi, H. Afshin, D. Dias, H. Jeong, 3D numerical study of the joint dislocation and spacing impacts on the damage of tunnel segmental linings, Structures *56* (2023) 104878, https://doi.org/10.1016/j.istruc.2023.104878.

[55] M. Zhao, J. Li, Y.M. Xie, Effect of vibration time on steel fibre distribution and flexural behaviours of steel fibre reinforced concrete with different flowability, Case Stud. Constr. Mater. *16* (2022) e01114, https://doi.org/10.1016/j.cscm.2022.e01114.

[56] BS EN 12390–3:2019. Testing hardened concrete — Compressive strength of test specimens. British Standards Institution, London, UK, 2019.

[57] BS EN 12390–5:2019. Testing hardened concrete — Flexural strength of test specimens. British Standards Institution, London, UK, 2019.

[58] BS EN 12390–6:2023. Testing hardened concrete — Tensile splitting strength of test specimens. British Standards Institution, London, UK, 2023.

[59] T. Jankowiak, T. Łodygowski, Identification of parameters of concrete damage plasticity constitutive model, Found. Civ. Environ. Eng. *6* (2005) 53–69.

[60] J. Lubliner, J. Oliver, S. Oller, E. Oñate, A plastic-damage model for concrete, Int. J. Solids Struct. *25* (1989) 299–326, https://doi.org/10.1016/0020-7683(89)90050-4.
[61] Smith, M. ABAQUS/Standard User's Manual, version 6.9, 2009.
[62] N.T. Nguyen, T.T. Bui, Q.B. Bui, Fiber reinforced concrete for slabs without steel rebar reinforcement: assessing the feasibility for 3D-printed individual houses, Case Stud. Constr. Mater. *16* (2022) e00950, https://doi.org/10.1016/j.cscm.2022.e00950.
[63] İ.B. Topçu, M. Canbaz, Effect of different fibers on the mechanical properties of concrete containing fly ash, Constr. Build. Mater. *21* (2007) 1486–1491, https://doi.org/10.1016/j.conbuildmat.2006.06.026.
[64] N. Srinivasa Rao, P. Rama Mohan Rao, P. Jagadeesh, Experimental evaluation of strength properties of steel fibre reinforced concrete, Asian J. Civ. Eng. *17* (2016) 487–494.
[65] K. Wille, D.J. Kim, A.E. Naaman, Strain-hardening UHP-FRC with low fiber contents, Mater. Struct. *44* (2011) 583–598, https://doi.org/10.1617/s11527-010-9650-4.
[66] D.Y. Yoo, Y.S. Yoon, Structural performance of ultra-high-performance concrete beams with different steel fibers, Eng. Struct. *102* (2015) 409–423, https://doi.org/10.1016/j.engstruct.2015.08.029.
[67] P.S. Song, S. Hwang, Mechanical properties of high-strength steel fiber-reinforced concrete, Constr. Build. Mater. *18* (2004) 669–673, https://doi.org/10.1016/j.conbuildmat.2004.04.027.
[68] F. Altun, T. Haktanir, K. Ari, Effects of steel fiber addition on mechanical properties of concrete and RC beams, Constr. Build. Mater. *21* (2007) 654–661, https://doi.org/10.1016/j.conbuildmat.2005.12.006.
[69] S.H. Chu, L.G. Li, A.K.H. Kwan, Fibre factors governing the fresh and hardened properties of steel FRC, Constr. Build. Mater. *186* (2018) 1228–1238, https://doi.org/10.1016/j.conbuildmat.2018.08.047.
[70] J. Han, M. Zhao, J. Chen, X. Lan, Effects of steel fiber length and coarse aggregate maximum size on mechanical properties of steel fiber reinforced concrete, Constr. Build. Mater. *209* (2019) 577–591, https://doi.org/10.1016/j.conbuildmat.2019.03.086.
[71] G. Schnüntger, E. Erdem, Brite-Euram Program on Steel Fibre Concrete, Subtask: Splitting of SFRC Induced by the Local Forces, Ruhr-University, Bochum, Germany, 2001.
[72] A. Nogales, A. de la Fuente, Crack width design approach for fibre reinforced concrete tunnel segments for TBM thrust loads, Tunn. Undergr. Sp. Technol. *98* (2020) 103342, https://doi.org/10.1016/j.tust.2020.103342.
[73] L. Zhou, Investigation of bursting stress and spalling stress in post-tensioned anchorage zones, Int. J. Concr. Struct. Mater. *15* (2021) 51, https://doi.org/10.1186/s40069-021-00490-9.
[74] L. Zhang, X. Liu, Experimental investigation of the deformed stagger-jointed segmental tunnel linings strengthened by epoxy-bonded filament wound profiles, Materials *15* (2022) 6862, https://doi.org/10.3390/ma15196862.
[75] S.H.P. Cavalaro, C.B.M. Blom, J.C. Walraven, A. Aguado, Structural analysis of contact deficiencies in segmented lining, Tunn. Undergr. Sp. Technol. *26* (2011) 734–749, https://doi.org/10.1016/j.tust.2011.05.004.74.
[76] S.H.P. Cavalaro, C.B.M. Blom, J.C. Walraven, A. Aguado, Formation and accumulation of contact deficiencies in a tunnel segmented lining, Appl. Math. Model. *36* (2012) 4422–4438, https://doi.org/10.1016/j.apm.2011.11.068.
[77] A. Ruttner, J. Stöcklin, Generalized tectonic map of Iran, Geological Survey of Iran (1968).
[78] Iranian Oil Operating Companies, Gachsaran Geological Map 1:100,000 (1996).